Journal of Colloid and Interface Science 542 (2019) 308–316

Contents lists available at ScienceDirect

Journal of Colloid and Interface Science

journal homepage: www.elsevier.com/locate/jcis

Regular Article

Multifunctional spiky branched gold-silver nanostars with near-infrared and short-wavelength infrared localized surface plasmon resonances

Dickson Joseph [a,*], Rengarajan Baskaran [c], Su Geun Yang [c], Yun Suk Huh [b,*], Young-Kyu Han [a,*]

[a] Department of Energy and Materials Engineering, Dongguk University, Seoul, Republic of Korea
[b] Department of Biological Engineering, Inha University, Incheon, Republic of Korea
[c] College of Medicine, Inha University, Chungsuk Bldg., Seohae-Daero, Jung-Gu, Incheon 22332, Republic of Korea

GRAPHICAL ABSTRACT

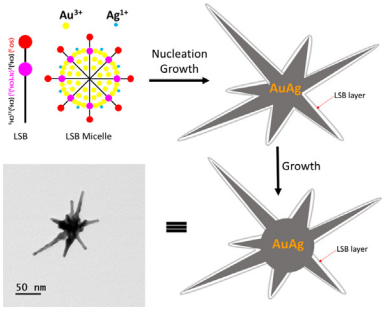

ARTICLE INFO

Article history:
Received 28 November 2018
Revised 30 January 2019
Accepted 31 January 2019
Available online 7 February 2019

Keywords:
Nanostar
Spiky Branched Nanostructure
Gold-Silver
Lauryl sulfobetaine
SERS
Photothemal
Nanocatalysts

ABSTRACT

We report a one-pot seedless green method for the synthesis of gold-silver (AuAg) spiky branched nanostars, with gold (90%) being the major component. Here, the zwitterionic surfactant lauryl sulfobetaine (LSB) is employed in the synthesis of bimetallic nanostars. The concentration of LSB plays an important role in determining the shape of nano-objects. A minimum LSB concentration of 50 mM is required for the formation of spiky branched nanostars, the size of which is controlled by increasing the LSB concentration. Two distinct intense localized surface plasmon resonances in the near-infrared (NIR) and short-wavelength infrared ranges are observed. The molecular structure of LSB causes LSB molecules to assemble into spherical micelles that act as a soft template for the growth of the nano-objects. An analysis of the mechanisms behind the formation of the nanostars suggests that there is a rapid growth of spikes followed by the formation of a spherical core at the center. AuAg nanostars with evenly spaced spikes and low branching demonstrate great potential as efficient nanocatalysts, surface-enhanced Raman scattering-active substrates and for photothermal therapy, active in both the visible and NIR regions.

1. Introduction

Plasmonic noble metal nanoparticles such as gold and silver show great potential for optical and biomedical applications due to their unique optical properties that arise from localized surface plasmon resonances (LSPRs) [1,2]. These resonances are strongly influenced by the anisotropy of the particles because most of these

Abbreviations: Au, gold; Ag, silver; NSs, nanostars; NP, nanoparticle; LSB, lauryl sulfobetaine; NIR, near-infrared; SWIR, short-wavelength infrared FETEM, field emission transmission electron microscope; EDX, energy-dispersive X-ray spectroscopy; AA, ascorbic acid; NaOH, sodium hydroxide; SERS, surface-enhanced Raman scattering; PTT, photothermal therapy.

* Corresponding authors.
E-mail addresses: josephdixon1979@dongguk.edu (D. Joseph), yunsuk.huh@inha.ac.kr (Y.S. Huh), ykenergy@dongguk.edu (Y.-K. Han).

https://doi.org/10.1016/j.jcis.2019.01.132
0021-9797/

particles exhibit LSPR peaks in the visible to near infra-red (NIR) regions [3,4]. The order of anisotropy predominates in branched nano-objects, which have been referred to as nanostars, nano-urchins, nanoflowers, and spiky, thorny or multibranched nanoparticles in previous research [5–10]. Branched nano-objects have generated significant interest for use in biological applications due to their tunable LSPR in the NIR region, within which blood and tissue are transparent [5,10]. Furthermore, due to the presence of multiple hot spots that arise due to the sharp protruding tips that confine and enhance a local electromagnetic field, this type of nanoparticle (NP) holds significant promise for use in surface-enhanced Raman scattering (SERS) and catalysis [11–15]. The core of a branched nanostructure serves as a nanoscale antenna that provides high charge density and charge polarization at the small radii tip of the spikes, enhancing the excitation cross section and the local electromagnetic fields [7,16,17].

Due to their unique properties, there has been an increasing number of synthetic procedures proposed for the controlled synthesis of branched nano-objects. Of particular interest is colloidal synthesis, which commonly involves either seeded growth or non-seeded homogeneous nucleation [3,8]. The seeded growth method consists of a two-step reduction process where small spherical NPs are initially prepared as seeds and added to a growth solution. Which usually contains silver ions (Ag+) to facilitate symmetry breaking [18], a weak reductant, shape-directing agents, and additional gold ions for the growth of nano-objects. In non-seeded growth, reduction is performed in a single step in which both nucleation and growth take place together. The materials required for the preparation of anisotropic NPs using non-seeded method are usually the same as those present in the growth solution used in the seeded method.

In various applications, including photothermal therapy, branched gold nanostructures are particularly common due to the low reactivity of gold [19]. Silver nanoparticles, on the other hand, are generally unstable and prone to intense, rapid oxidation [20]. However, they are also excellent plasmonic materials and can sometimes produce a stronger plasmonic resonance than their gold counterparts, especially in SERS applications [21,22]. Hence, incorporating a fraction of silver with gold as an alloy is an effective way to enhance the optical properties of gold while preserving its biocompatibility. In addition, due to the bi-functional or synergistic effects produced by metal-to-metal charge transfer, nanoalloys exhibit superior properties when compared to their constituent monometallic elements [23]. The goal of this work is thus to prepare bimetallic gold-silver branched nano-objects using a simple one-pot synthetic protocol.

In recent years, the non-seeded one-pot synthesis of branched nano-objects has been investigated as a way to overcome the complications involved in two-step seeded growth [24–26]. However, there has been a lack of reports on nano-objects with longer and sharper multibranched structures (something which has not been achieved using the seeded-growth method either) that can efficiently enhance electromagnetic fields. Therefore, we propose a one-pot method for the high-yield synthesis of branched nano-objects with varying branch numbers and lengths, which we refer to as nanostars. Nanostars are nano-objects with spikes protruding from a spherical core. Synthesis is achieved using aqueous wet chemistry method in the presence of the zwitterionic surfactant lauryl sulfobetaine (LSB). The critical micelle concentration (CMC) of LSB is 2 mM, at which it forms spherical micelles [27,28]. LSB consists of a sulfate anion and a quaternary ammonium cation separated by a short methylene spacer as the hydrophilic polar headgroup and a hydrocarbon chain as the hydrophobic tail [29].

The synthesis of gold nanostars using the seeded-growth method in the presence of LSB has been reported previously [28,30], but their yield and uniformity have been poor using this multi-step process. We are able to optimize the synthetic protocol to control the number of branches and their length by varying the concentration of LSB. In addition, because sulfobetaines are a series of commercially available zwitterionic surfactants with varying hydrophobic hydrocarbon chain lengths, two other sulfobetaines with different chain lengths, octyl sulfobetaine (OSB) and palmityl sulfobetaine (PSB), were also examined under similar conditions to study the influence of the surfactant on the shape of the resulting nanostars. In contrast to previously reported studies on the preparation of nanostars, we report here the preparation of bimetallic AuAg nanostars. We compare the effect of the three zwitterionic surfactants on nanostructure formation and determine the formation mechanisms based on time-resolved transmission electron microscopy (TEM). Exploiting the localized surface plasmon resonance effects of plasmonic nano-objects holds the key to their enhanced performance in various applications. Hence, here we assess the properties of the as-prepared bimetallic AuAg nanostars by investigating their catalytic activity and surface-enhanced Raman scattering (SERS) effects.

The potential use of our proposed nanostars in photothermal therapy (PTT) is also explored in this study. PTT is a minimally invasive therapeutic approach that converts photon energy into heat energy to destroy cancer cells [31,32]. PTT is based on the NIR-light irradiation of nanomaterials such as gold, quantum dots, carbon nanotubes, and graphene oxide, which leads to the excitation of the nanomaterial and the dissipation of the heat to the surrounding area [33–36]. In particular, anisotropic noble metal nanoparticles can be directly and effectively delivered to the target sites and NIR photon radiation applied at a range between 700 and 1400 nm in continuous or pulsed modes to avoid damage to the normal cells [3], with the wavelength of the emitted photons affected by the size and shape of the nanoparticles. The high absorbance of our as-prepared AuAg nanostars in the NIR region is expected to be transformed into highly stable heat generation in a biological environment, thus making them potentially useful in this treatment. Indeed, biomedical science is currently facing the serious challenge of drug-resistant cancer cells and microbial pathogens, which can be overcome by engineering plasmonic nanostructures such as nanostars [25,37–40]. The treatment of drug-resistant health conditions using PTT is thus important because it represents a drug-free, cost-effective treatment method.

2. Experimental section

2.1. Materials and methods

All of the reagents used in this study were of analytical reagent grade. Hydrogen tetrachloroaurate(III) trihydrate ($HAuCl_4{\cdot}3H_2O$), silver nitrate ($AgNO_3$), ascorbic acid (AA), 4-nitrophenol (4-NP), sodium borohydride ($NaBH_4$) and 4-aminothiophenol (4-ATP) were purchased from Sigma-Aldrich. Lauryl sulfobetaine (LSB), octyl sulfobetaine (OSB) and palmityl sulfobetaine (PSB) were purchased from Tokyo Chemical Industry Co., Ltd. (Korea), and sodium hydroxide (NaOH) was purchased from Samshun Pure Chemical Co., Ltd. (Korea). All chemicals were used as received. Doubly distilled deionized (DI) water (H_2O) was used throughout the synthesis process. All glassware was precleaned with aqua regia (a mixture of HCl:HNO_3 at a 3:1 vol ratio) and rinsed thoroughly with DI H_2O. The morphology of the nano-objects was observed using a JEM-2100F (JEOL, Japan) field emission transmission electron microscope (FETEM) operated at a voltage of 200 kV and equipped with an energy-dispersive X-ray spectrometer (EDS, Oxford Instruments, Oxford, UK) for elemental analysis. For FETEM imaging, the synthesized colloids were concentrated by centrifuging at 8000 rpm for 10 min, collecting the residue, and dispersing it in

1 mL of H_2O. The concentrated solution was dropped onto a carbon-coated copper grid and dried in a vacuum for 24 h before imaging. UV–Visible-NIR spectra for the as-prepared colloidal solutions were recorded using an UV–Visible-NIR spectrophotometer (V-770 Jasco, Japan).

2.2. Synthesis of the gold-silver nanostars

The standard synthesis process in this study was carried out in 10 mL batches, with appropriate volumes of LSB dissolved in DI H_2O (8.45 mL) under stirring in a 70 mL glass vial to produce 25, 50, 75, and 100 mM LSB. After complete dissolution, the stirring was halted and $HAuCl_4{\cdot}3H_2O$ (0.5 mL, 0.01 M) added to the LSB solution, followed by mixing using manual agitation. $AgNO_3$ (0.05 mL, 0.02 M) was also added and mixed again using manual agitation for about 1 min. Finally, NaOH and AA (0.1 mL, 0.1 M) were added and mixed until a blackish color was observed. The mixture was then left undisturbed under ambient conditions for 12 h to allow the gold-silver nanostars (AuAg NSs) to form. For larger volumes of LSB, the amounts of DI H_2O, metal precursors, NaOH, and AA were increased proportionally.

2.3. Catalytic reduction of 4-Nitrophenol using AuAg nanostars

Prior to each experiment, a 4-NP and $NaBH_4$ solution was freshly prepared. $NaBH_4$ (150 μL, 0.1 M) and AuAg NS (50 μL) were sequentially added to an aqueous solution of 4-NP (30 μL, 0.01 M) in a 3 mL disposable UV cuvette containing 2.77 mL of H_2O and then mixed. Time-resolved UV–Vis absorbance spectra were recorded using a UV–Vis spectrometer at 1-min time intervals with a 200–800 nm wavelength scanning range under ambient conditions.

2.4. Surface-Enhanced Raman spectroscopy measurements

Raman spectroscopy (FEX, NOST, Republic of Korea) measurements were all performed at an excitation wavelength of 785 nm. Top-view spectra were collected (laser power: 60 μW, accumulation time: 15 s) using a 100X objective. SERS measurements were performed with 1 mM, 4-aminothiophenol (4-ATP) as a SERS probe molecule. The as-prepared AuAg NSs were washed via centrifugation at 8000 rpm for 10 min, followed by the redispersion of the residue in 1 mL of DI water. From this colloidal solution, 50 μL of the NCs were dispersed in 0.45 mL of ethanolic 4-ATP solution and left to stand under ambient conditions for at least 6 h to allow probe-molecule adsorption by the nanostars. The samples were then centrifuged to remove the unbound 4-ATP molecules and the residue washed an additional two times with absolute ethanol to remove any excess unbound 4-ATP. The residue was then re-dispersed in 50 μL of ethanol and the solution dropped onto a Si wafer and dried in the air in preparation for SERS measurements.

2.5. Photothermal studies

In the first set of experiments, three aqueous solutions containing AuAg NSs of different sizes were placed in a glass vial and irradiated from the top with an 808 nm diode laser with an energy of 200 mW/cm^2. The best performing sample in this experiment (AuAg NS50) was selected and then irradiated from the top at different energy densities (50, 100, 200, and 500 mW/cm^2) using the 808 nm diode laser. This was followed by further characterization at 200 mW/cm^2 using irradiation from a 680-nm diode laser. An NIR camera was placed and focused on the point of laser exposure and images were recorded at specific time intervals. The thermographs were analyzed using IR Flash software to obtain the average temperature of the AuAg NS solution.

3. Results and discussion

A one-pot synthetic method designed to replace the commonly used galvanic replacement reaction method [41] for the synthesis of AuAg hollow cubic nanostructures was recently developed and reported by us [42]. Micelles of the biocompatible surfactant Tween 80 (T80) were used as soft templates for the growth of the hollow nanocubes and ascorbic acid (AA) was employed as the reducing agent. Here, we describe a simple one-pot seedless method for the synthesis of AuAg nanostars (AuAg NSs) using a modified synthetic process in the presence of the zwitterionic surfactant lauryl sulfobetaine (LSB). To identify the optimal experimental conditions for the synthesis of nanostructures, UV–Vis-NIR spectroscopic measurements were used as the primary screening characterisation tool in conjunction with TEM analysis. Replacing T80 with LSB, experiments were performed that combined gold and silver metal ions at a 5:1 ratio in the presence of AA.

Fig S1 shows the UV–Vis-NIR extinction spectra of three different concentrations (25 mM, 50 mM and 75 mM of LSB) and TEM images of the AuAg NSs obtained in the presence of 50 mM LSB. The plasmon bands in the NIR region for all three concentrations suggest the formation of non-spherical nano-objects and the broadness of these bands indicates non-uniformity in size and shape. Due to the similarities in the plasmon bands, the AuAg NSs synthesized using 50 mM LSB were examined as a model sample using TEM; they were observed to have formed of large star-shaped non-uniform aggregates. AA (pKa1: 4.10, pKa2: 11.79) is known to possess poor reduction ability at low pH. However, the ability to reduce metal ions increases with increasing pH [43]. We speculate that the non-uniform size and shape of the AuAg NSs formed here could be the result of the poor reduction ability of AA. Hence, the reaction was performed under alkaline conditions using equimolar proportions of AA and NaOH. Five different concentrations (10, 25, 50, 75, and 100 mM) of LSB were examined to investigate the effect of concentration on AuAg NS formation. Well dispersed colloids of excellent stability comparable to the parent nanoparticles were obtained. As shown in the UV–Vis-NIR results (Fig. 1), differences in plasmon bands were observed for the five LSB concentrations. A single plasmon band at 527 nm for 10 mM LSB clearly indicates the formation of spherical AuAg NSs. As the concentration of LSB increased, a hypsochromic shift in

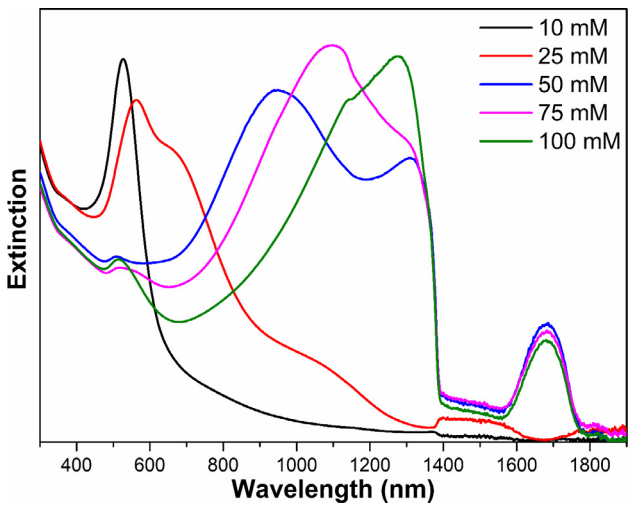

Fig. 1. UV–Vis-NIR extinction spectra of nano-objects formed at different concentrations of LSB.

the plasmon bands to the NIR region was observed, suggesting the formation of non-spherical AuAg NSs. For 25 mM LSB, strong absorption was observed at 563 nm and two shoulder peaks were observed centered around 670 nm and 1054 nm, indicating the evolution of non-spherical particles. Above a concentration of 50 mM LSB, maximum absorption occurred in the NIR region, exhibiting distinct narrow plasmon bands in contrast to the broad bands observed when only AA was used. For example, in the 50 mM LSB samples without NaOH, a broad plasmon band centered at 1200 nm was observed. When NaOH was added, the broad band split into two narrow bands, with one positioned at 949 nm and the other at 1308 nm (Figs. S1A and 1). The distinct narrowing of the bands suggests the formation of AuAg NSs of uniform size and well-defined shape. As the concentration of LSB increased further to 75 and 100 mM, the two distinct peaks observed at 50 mM merged into a single peak positioned at 1098 nm and 1278 nm, respectively. The hypsochromic shift in the plasmon bands from 527 nm for 10 mM LSB to 1278 nm for 100 mM LSB also suggests an increase in the size of the AuAg NSs.

The results of the TEM analysis coincide with the extinction spectra for the different concentrations of LSB. As shown in Fig. 2, the AuAg NSs formed using 25 mM LSB were small star-shaped (25 ± 4 nm) and appeared similar to spherically shaped nano-objects under low magnification. Above 50 mM, AuAg NSs with a well-defined star shape were observed, with an increase in the size and the number of branches with increasing LSB concentration. The radius of the star was used as a measure to define the size of the AuAg NSs by calculating the distance from the center of the star to the edge of the branchs. The average size of the AuAg NSs measured from the TEM images using ImageJ software was found to be 69 ± 13 nm, 88 ± 17 nm, and 107 ± 16 nm for LSB concentrations of 50 mM, 75 mM, and 100 mM, respectively.

STEM-EDX mapping was used to assess the distribution of Au and Ag elements in the NS (Fig. S2). The EDX results show that the weight percentage of Au at the center and the edge was above 85% (92:8 and 89:11, respectively), suggesting that the major portion of the AuAg NSs were made up of Au. There was a minor difference in the atomic ratio of Au:Ag at the centers and edges (87:13 and 82:18 respectively). The above elemental mapping, conducted using point patterns, suggests that the elemental ratio between Au and Ag is 6:1 at the centre and 4.5:1 at the edge, which is close to the feed ratio of 5:1. The ratio obtained using inductively coupled plasma optical emission spectrometry (ICP-OES) was 7:1. Thus, the oxidation state of Au and Ag on cubic nanostars exists in the form of elemental Au and Ag rather than their ions, confirming the complete reduction of metal ions to metal with a ratio close to the feed ratio.

To study the role of Ag in the formation of the nanostars and to understand the mechanisms involved in this process, experiments were performed using four ratios of Au to Ag (5:0, 5:1, 5:5 and

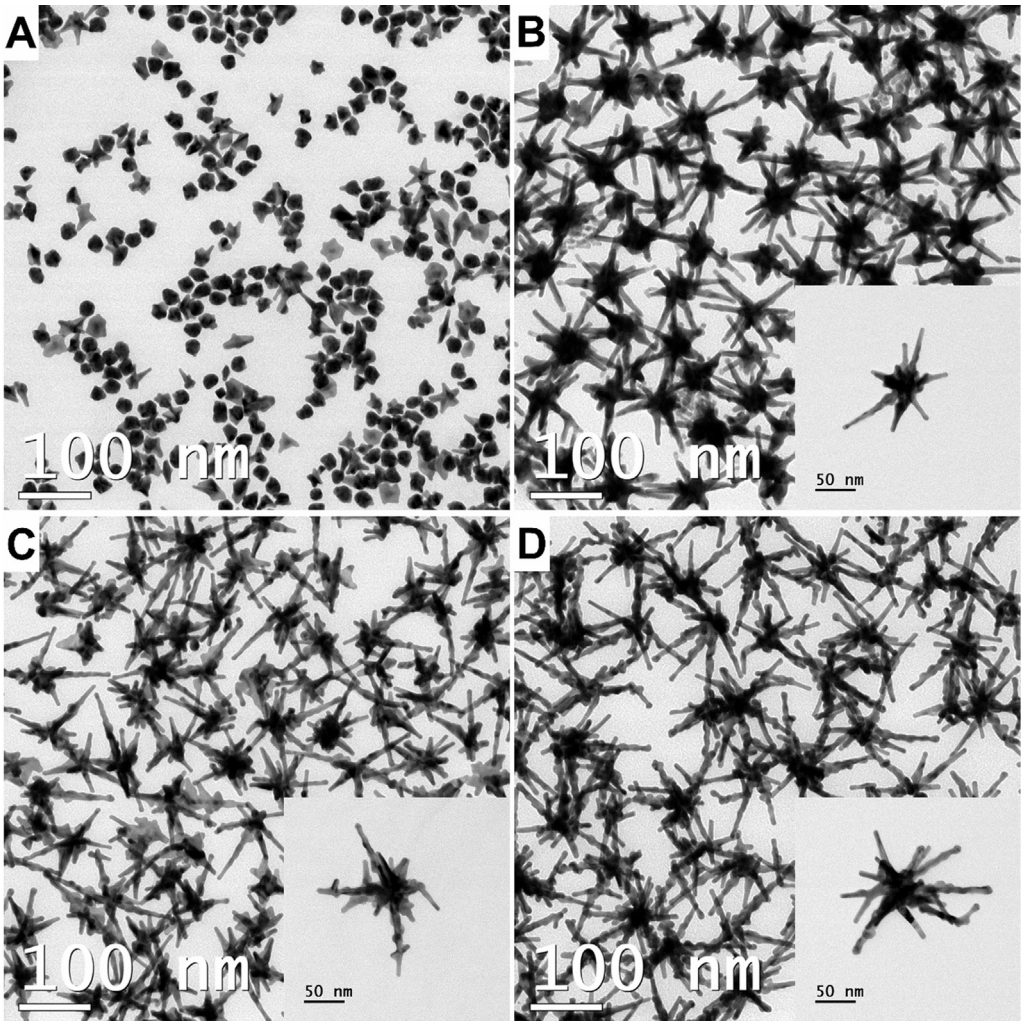

Fig. 2. TEM images of nano-objects formed at different concentrations of LSB: (A) 25 mM, (B) 50 mM, (C) 75 mM and (D) 100 mM. Scale bar = 100 nm. Insets represent the corresponding single nanostar.

5:10) with 50 mM LSB. UV–Vis-NIR analysis (Fig. S3) confirmed a sharp peak at 538 nm and a broad shoulder in the NIR region for the 5:0 ratio, indicating the formation of randomly shaped NPs with a broad range of sizes. As the concentration of Ag in the reaction system increased, bathochromic shifts in the LSPR bands were observed, indicating a decrease in the size of the NPs. In addition, a decrease in the intensity of the band at 1684 nm was observed. To examine the shape and the size of the NPs under these conditions, TEM analysis was conducted. As shown in Fig. S3, there was a change in the morphology of the nanostars and a decrease in size (69 ± 13 nm, 39 ± 7 nm, and 17 ± 9 nm for the ratios of 5:1, 5:5 and 5:10, respectively). For the 5:0 ratio, we observed solid NPs with multiple shapes and an average size of 77 ± 19 nm. From the above analysis, it is clear that the presence of a low feed concentration of Ag is crucial to the formation of star-shaped nano-objects. However, a high concentration of Ag leads to nano-objects that are close to spherical. We postulate that, as the concentration of Ag in the system increases beyond that of Au, the reduction of Ag ions takes place faster than for the Au ions, thus the ability of Ag ions to break the symmetry of the initial NPs is lost.

Overall, we can confirm that reducing the AuAg metal ions at a 5:1 ratio in the presence of equimolar AA, NaOH, and LSB concentrations above 50 mM, AuAg NSs can be obtained. The size and the number of the branches are controlled by the concentration of LSB. This leaves us with the question of what mechanisms are involved in the formation of AuAg NSs in the presence of LSB. We believe that the micellar structure formed in an aqueous medium in the presence of Au and Ag metal salts and the reducing agents plays a major role in directing the shape of NPs. To confirm this role of the micellar structure, we performed the same experiments using other zwitterionic surfactants to determine if similar AuAg NSs could be obtained. Two sulfobetaine surfactants with differences in their hydrophobic chain were selected: octyl sulfobetaine (OSB; CMC = 330 mM), which contains two CH_2 groups fewer in its hydrophobic chain than LSB, and palmityl sulfobetaine (PSB; CMC = 0.01 mM), which has two additional CH_2 groups. Experiments were performed under the same protocol in the presence of the corresponding surfactants (50 mM). As a preliminary observation, we found that the colloid obtained using OSB was reddish in color, while PSB produced a bluish colloid which soon aggregated and settled at the bottom, indicating poor stability (Fig. S4C). UV–Vis-NIR and TEM analysis of OSB indicates the formation of small non-uniformly shaped nano-objects that resembled the AuAg NSs (Fig. S4). However, although we used the same class of zwitterionic surfactants to which LSB belonged, we were not able to obtain the same star-shaped NPs. Hence, it is clear that the micellar structure that a particular surfactant forms in the reaction medium determines the shape of the nano-objects at the end of the reaction. We believe that, at concentrations of LSB at or above 50 mM, a micellar structure that favours star-shaped NPs is formed in the aqueous reaction medium.

Time-resolved UV–Vis-NIR spectroscopy and TEM analysis of the AuAg NSs obtained using 50 mM of LSB were conducted to understand the evolution of NP shape and the mechanisms behind it. The reactants were added as described in the experimental section in a vial. After the appearance of the blackish coloration, 1 mL of the sample was taken and placed in a UV quartz cuvette. Absorbance was measured without disturbing the sample in cycles until maximum intensity had been achieved. As shown in Fig. S5, upon addition of the reducing agents to the surfactant solution with the metal ions, reduction takes place instantaneously. LSPR bands characteristic of anisotropic NPs were observed from the UV to the NIR region. A weak band at 532 nm, the strongest band at 935 nm, a shoulder band at 1306 nm, and a strong band at 1684 nm were observed. After one hour, the intensity of the bands increased, with a slight hypsochromic shift in the band at 935 nm to 910 nm and a bathochromic shift in the band at 1306 nm to 1314 nm. The bands at 532 nm and 1684 nm remained unchanged. As time progressed further, the band at 910 nm narrowed and exhibited a hypsochromic shift until it reached a stable point after 6 h, after which there was no change observed in any of the bands. These results indicate that nucleation and growth take place instantly within an hour and further definition of the shape of the NPs takes place over the course of 6 h.

The change in the shape of the NPs was observed from images taken at different intervals of time using TEM, based on the above time-dependent UV–Vis-NIR experiment. Four samples were prepared, and the reaction was arrested using centrifugation to remove the unreacted reactants at different intervals of time: 0 h (soon after the addition of the reducing agents), 1 h, 3 h, and 6 h. The centrifuged precipitate was concentrated and dropped on a TEM grid. The TEM image in Fig. S6 identifies the formation of NPs with branches protruding from its center point. Over the course on an hour, the core of the branched NPs surrounding the center point where the branches originated grew into a thicker spherical structure, eventually leading to the formation of star-shaped NPs with a spherical core and branches protruding from the center of the core. After 1 h, there was no significant change is the shape of the NPs. Based on the UV–Vis-NIR and TEM analyses, we believe that the LSPR band at 1684 nm corresponds to the branches in the NPs because the band was first observed within a few minutes of the reaction beginning, and it remained unchanged throughout. The other bands correspond to the core of the NPs, which was weak in the early stages of the reaction intensified after 1 h, as indicated by the TEM images.

Overall, from the above observations, we can propose the mechanisms that lead to the formation of AuAg NSs in the presence of different surfactant concentrations. A schematic representation of the formation of star-shaped NPs using 50 mM LSB is presented in Fig. 3. Initially, when LSB is dissolved in water, it forms spherical micelles, with the head of the surfactant molecules pointing outwards and the tail inwards towards the core [44]. Upon the addition of the $HAuCl_4$ salt, the Au^{3+} ions assemble around the stern layer (head group region of the LSB micelle [44]. Similarly, when $AgNO_3$ is added, the Ag^+ ions distribute themselves over the Au^{3+} ions around the head group of the surfactant micelle. When the reducing agents AA and NaOH are added to the surfactant solution with the metal ions, nucleation takes place very rapidly leading to the formation of small spherical AuNPs and AgNPs. The AgNPs break the symmetry of the AuNPs, allowing additional Au ions to interact with the nuclei and generating further growth into anisotropic NPs. At a 5:1 ratio of Au:Ag, the Ag ions are distributed at defined positions far from each other. The AgNPs are able to break the symmetry of the AuNPs at those positions, and it is only at these positions that the anisotropic growth of AuNPs takes place, leading to protrusions at these spots that grow into branches. The remaining Au ions that are not involved in the branching are reduced at the center of the branches that lead to the thick spherical core. This finally results in NPs with sharp protrusions from a thick spherical core (i.e., AuAg NSs).

In Fig. S3, it can be observed that higher concentrations of Ag led to NPs that were almost spherical in shape. This supports our proposed synthesis mechanism described above. When the Au:Ag ratio is 1:1, there is an equal distribution of metal ions, and the Ag ions are closer to each other. The AgNPs thus become involved in the nucleation process together with the AuNPs, rather than facilitating the breaking of symmetry at defined points. Therefore, the presence of excess Ag ions interferes with the interaction between the Au nuclei and Au ions, obstructing the growth of anisotropic AuNPs and leading to NPs that resemble spheres. As a result, the 5:1 ratio of Au to Ag is crucial in the formation of

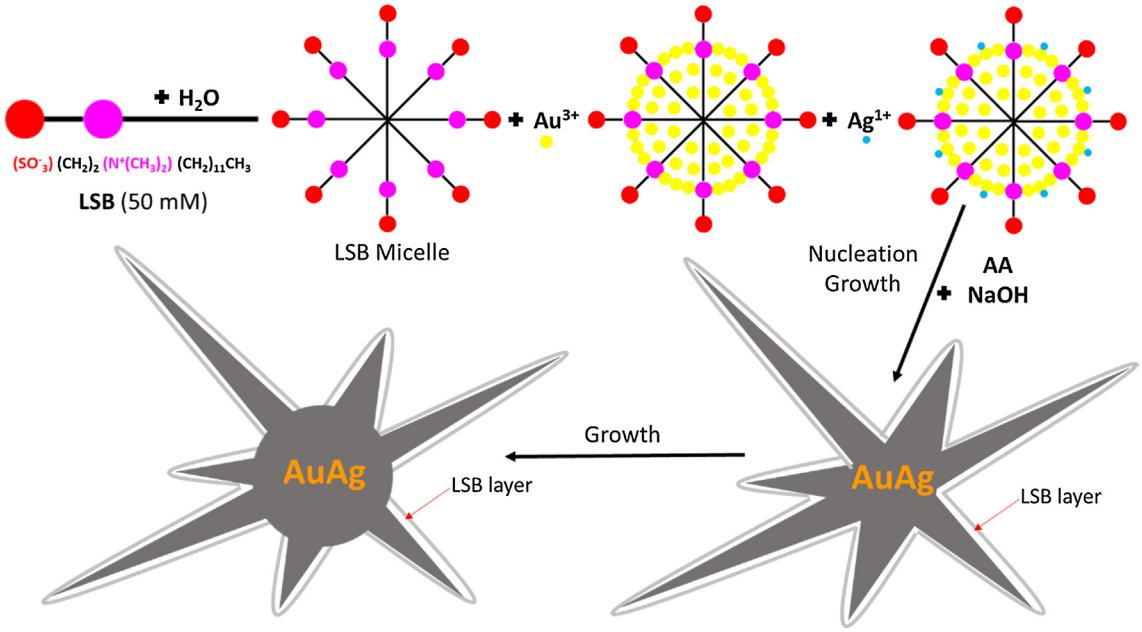

Fig. 3. Schematic representation of the proposed micelle formation process using 50 mM LSB and the nanostars that are expected to grow over the micelles.

star-shaped NPs because Ag plays a dominant role in the formation of the branching that protrudes from the core of the NPs. Without Ag or with excess Ag, only solid, randomly shaped NPs that resemble spheres can be observed (Fig. S3).

The concentration of LSB plays an important role in controlling the size of the AuAg NSs (Fig. 2). The NPs formed in the presence of 25 mM LSB are small and star-shaped (25 ± 4 nm) and appear similar to spherically shaped NPs under low magnification. Above 50 mM, well-defined star-shaped NPs are observed, with an increase in the size and number of branches. It is believed that, at an LSB concentration of 50 mM, micelles as presented in Fig. 3 are formed, leading to the formation of the NPs described above. As the concentration of LSB increases to 100 mM, the size of the micelles also increases due to an increase in the minimum number of molecules that constitute a micelle (i.e., the aggregation number) [44]. As shown in Fig. S7, due to the higher concentration of LSB molecules in the system, the packing of the molecules in the LSB is higher. A dense micelle allows for the arrangement of more metal ions around the micellar structure, which, when nucleated, grows into a larger NP with a higher number of branches. The opposite behavior was observed for 25 mM LSB, where less dense micelles form in the aqueous solution because of the lower aggregation number. Due to the lower concentration of LSB, the interaction between the nuclei and the metals is much easier and more rapid. This leads to the formation of NPs with a spherical shape rather than anisotropic NPs, which require a slower reaction rate. This means that an optimal 50 mM concentration of LSB is required to obtain well-defined AuAg NSs, the size and number of branches of which can be increased by increasing the concentration of LSB. In our previous study [42], when T80 was used in the synthesis of anisotropic NPs, we observed that, as the concentration of the surfactant increased, the NPs became smaller. For LSB, we observed the opposite relationship, in which an increase in the concentration of LSB led to NPs of increased size. Thus, it can be concluded that the mechanisms involved in the formation of NPs using different surfactants depends on the micellar structure that forms in that particular system.

The influence of the size and number of branches of three types of AuAg NSs obtained using different concentrations of LSB (50, 75, and 100 mM; referred to as AuAg NS50, AuAg NS75, and AuAg NS100, respectively) was examined based on catalytic activity, SERS, and photothermal efficiency (Fig. 2). The reduction of 4-nitrophenol (4-NP) by sodium borohydride ($NaBH_4$) in the presence of a catalyst was chosen as a model catalytic reaction to investigate the catalytic properties of the as-prepared AuAg NSs. The reduction process was monitored both visually and using UV–Vis spectroscopy. A typical 4-NP absorption band appeared at 317 nm, which demonstrated a [1]red shift to 400 nm upon addition of $NaBH_4$ due to the formation of 4-nitrophenoloate ions (Fig. 4). The concentrations of the reactants for the experiment were optimized at 30 μL of 0.01 M 4-NP, 150 μL of 0.1 M $NaBH_4$, and 50 μL of AuAg NSs as a catalyst. The concentration of the Au ions used for the synthesis was 0.5 mM, resulting in a final Au concentration of ~80 μM in the 3-mL catalytic reaction vessel. When the AuAg NSs were added, the sequential attenuation in the peak intensity at 400 nm was observed with increasing reaction time, with the gradual appearance of a new peak at 300 nm and an increase in intensity indicating the formation of 4-aminophenol (4-AP) [45]. The light-yellow color of the 4-NP solution changed rapidly to bright yellow with the addition of the $NaBH_4$ aqueous solution, indicating the formation of 4-nitrophenolate ions. Subsequently, with the addition of the catalyst, the color changes from bright yellow to light yellow to colorless due to the successive reduction of the 4-nitrophenolate ions to 4-AP. The catalytic reduction rate varied for the three types of AuAg NSs (Fig. 4). The catalytic activity decreased with an increase in the size and branching of the AuAg NSs, which could be attributed to their high effective surface areas [46]. The reduction times for AuAg NS sizes of 69 ± 13 nm (AuAg NS 50), 88 ± 17 nm (AuAg NS 75), and 107 ± 16 nm (AuAg NS 100) were 8, 13, and 20 min, respectively. The greater size and number of branches in AuAg NS100 were expected to increase the number of reaction sites, but steric hindrance was a factor in the adsorption of 4-NP molecules onto the AuAg NSs. However, the evenly distributed gaps between the spikes of AuAg NSs with less branching meant it was easier for the 4-NP molecules to adsorb onto the AuAg NSs, particularly at the core. Thus, due to the higher effective surface area of AuAg NS50,

[1] For interpretation of color in Fig. 4, the reader is referred to the web version of this article.

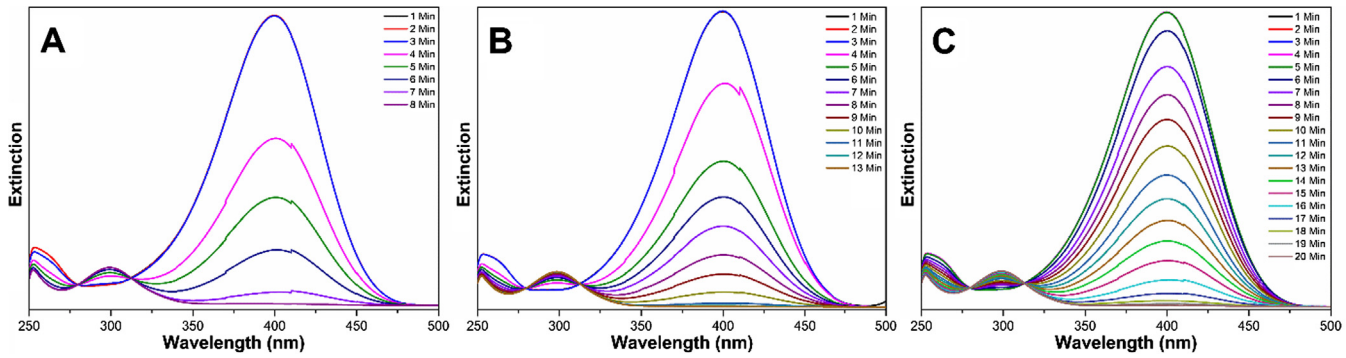

Fig. 4. UV–Vis extinction spectra recorded during the reduction reaction of 4-nitrophenol with $NaBH_4$ in the presence of 50 μL of (A) AuAg NS50, (B) AuAg NS75, and (C) AuAg NS100.

adsorption of 4-NP molecules onto the AuAg NSs was higher, resulting in more efficient catalytic activity compared to AuAg NS75 and AuAg NS100. We believe a nanocatalytic molecular reduction mechanism occurs in the same manner as that explained by Mahmoud et al. [47]. Initially, $NaBH_4$ reacts with water on the surface of the nanocatalyst to produce hydrogen and an oxidized form of borohydride. When a 4-NP molecule approaches the surface of the nanocatalyst, it is reduced by the adsorbed oxidized $NaBH_4$ species.

To confirm the importance of the size of the NPs and the effect of branching, we analyzed the SERS properties of AuAg NS50, AuAg NS75, and AuAg NS100. As in the previous analysis, AuAg NS50 exhibited the most advantageous SERS properties in comparison to the larger AuAg NSs with a higher number of branches. Fig. 5 presents the SERS sensitivity of the AuAg NSs using a 4-ATP (1 mM) ethanolic solution as an analyte. AuAg NS50, with its shorter branch length, had a number of SERS-active sites due to the short junctions between two adjacent NPs [48]. These junctions act as hot spots by efficiently transporting the intense local electromagnetic field from the NPs through the analyte molecules, in which highly efficient Raman scattering can be observed. On the other hand, for AuAg NSs with longer branches, the local electromagnetic field that originates from the spherical core fades as it reaches the tip of the branches or the junction between two adjacent NPs, leading to weaker SERS signals. Interestingly, AuAg NS75 and AuAg NS100 exhibited similar SERS effects to each other but not to AuAg NS50, indicating that they are similar in terms of size and branching (Fig. 2).

The photothermal efficiency of AuAg NSs was evaluated by measuring the increase in temperature under ambient conditions induced by irradiating aqueous solutions of AuAg NS50, AuAg NS75, and AuAg NS100 at a wavelength of 808 nm, which is close to the NIR LSPR. An elevation in temperature was observed for all three samples (Fig. 6A), while irradiating pure water and surfactant solutions with the same laser source at the same power did not show any increase in temperature. Again, AuAg NS50, with an average size of 69 ± 13 nm and less branching, demonstrated the best performance; following 300 s of irradiation, AuAg NS50, AuAg NS75, and AuAg NS100 exhibited temperature increases of 4.4 K, 4.1 K, and 3.6 K, respectively. This result can be explained in terms of localized light absorption by the AuAg NSs, their conversion of energy to heat, and subsequent dissipation of this heat to the surrounding environment. For AuAg NS50, the presence of open space between the spiky branches allowed for more light absorption by the spherical core. The heat can then be efficiently dissipated outwards into the surrounding environment through the spiky branches, which act as antennas. On the other hand, for AuAg NS75 and AuAg NS100 the penetration of the spherical core by the photons is hindered by the greater size and increased branching of the NPs, lowering their photothermal efficiency.

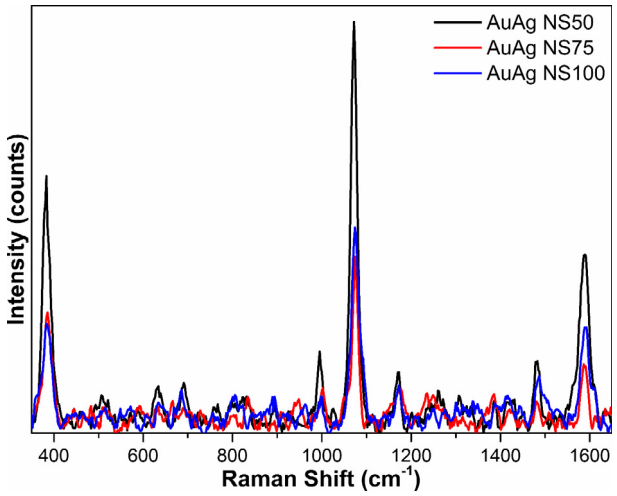

Fig. 5. Characteristic SERS spectra of 4-ATP on the as-prepared nanostars.

The change in temperature of AuAg NS50 as a function of laser intensity was then assessed at energy levels of 50, 100, 200, and 500 mW/cm^2 for an exposure time of 300 s. Fig. 6B illustrates that the temperature increased with higher energy levels. For 50 mW/cm^2, an increase of just 0.8 K was observed, but this rose to 1.6 K, 4.4 K, and 10 K for 100, 200, and 500 mW/cm^2, respectively. In particular, at a power density of 500 mW/cm^2, an initial sharp increase of 8.8 K was observed within 150 s, followed by a slower rise up to 10 K after 300 s. Due to the steady and gradual increase in the temperature of AuAg NS50 using a continuous wave 808-nm laser, the effect of a pulsed flow on the overall increase in temperature was analyzed as a comparison (Fig. 6C). We observed a lower rise in temperature (2.1 K) when a pulsed laser was used in comparison to the 4.4 K rise obtained with a continuous wave laser. It is interesting to note that there was no major drop in the temperature during the on/off intervals, with the temperature remaining above 298 K throughout the pulsed exposure time (300 s). Finally, to examine the effect of photothermal efficiency in the visible region, AuAg NS50 was irradiated with a 680-nm laser source at 200 mW/cm^2 for 300 s. We observed a rise in temperature of 4.1 K, which is similar to that for AuAg NS50 irradiated with an 808-nm laser (4.4 K). In summary, AuAg NS50 demonstrated the best performance due to the presence of evenly distributed gaps between the spikes that acted as antennas to efficiently dissipate the heat generated from the core of the NPs into the surrounding environment. These nanoparticles are expected to cause no toxicity issues when applied in the biomedical field or as industrial materials since they are stabilised by a

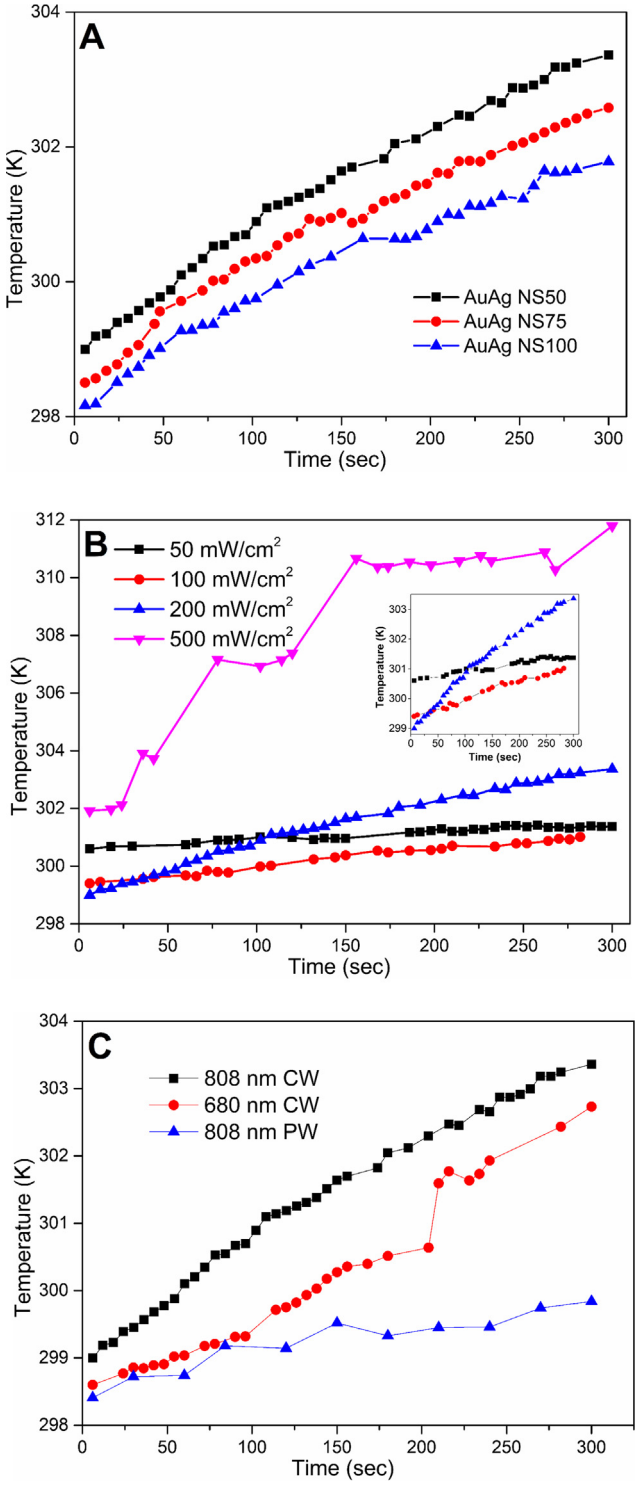

Fig. 6. (A) The NIR-induced temperature increase of nanostars prepared using different concentrations of LSB, (B) the NIR-induced temperature increase of AuAg NS50 at different power densities, and (C) a comparison of the temperature increase of AuAg NS50 using a visible range laser source (680 nm) and comparison between continuous wave and pulsed wave NIR laser sources (808 nm).

zwitter-ionic surfactant that is less toxic and safer surfactant than the cationic or anionic surfactants.

4. Conclusions

In this study, we report a one-pot seedless green synthetic method that involves the addition and manual mixing of precursors for the preparation of spiky branched gold-silver nanostars (AuAg NSs) whose size and branching can be controlled. Lauryl sulfobetaine (LSB) has been shown to effectively influence the formation of these AuAg NSs. The effect of LSB concentration on the shape of the AuAg NSs suggests that micelles play a role in this process. The spherical micellar structure is believed to act as a soft template for the formation of AuAg NSs. The concentration of silver ions plays a major role in breaking the symmetry of the gold nanoparticles (NPs) and facilitating the formation of protrusions from the central core. AuAg NSs are synthesized via the initial formation of these spikes followed by the formation of the spherical central core. The as-prepared AuAg NSs exhibited tuneable LSPRs in the NIR region (700–1400 nm) and a unique fixed LSPR that features in the SWIR region at 1684 nm. The AuAg NSs exhibited multifunctional properties, including acting as a nanocatalyst and a SERS-active substrate, as well as demonstrating photothermal activity. AuAg NSs with evenly distributed spikes and lower branching (AuAg NS50) displayed the best performance in these areas. The catalytic and SERS activity can be attributed to the presence of a large effective surface area and efficient electromagnetic field transport through the short junctions between adjacent NPs, respectively. The spikes of the AuAg NSs act as antennas in effectively dissipating the heat produced at the core to the surrounding environment following irradiation with a laser source. The AuAg NSs are photothermally active both in the visible and NIR regions.

Acknowledgments

This work was supported by the National Research Foundation of Korea (NRF) grant funded by the Korea government (MSIT) (No. 2014R1A5A1009799, 2017M2A2A6A01020938, and 2016R1A2B4013374).

Appendix A. Supplementary material

Supplementary data to this article can be found online at https://doi.org/10.1016/j.jcis.2019.01.132.

References

[1] N. Jiang, X. Zhuo, J. Wang, Active plasmonics: principles, structures, and applications, Chem. Rev. 118 (2018) 3054–3099.
[2] S. Unser, I. Bruzas, J. He, L. Sagle, Localized surface plasmon resonance biosensing: current challenges and approaches, Sensors 15 (2015) 15684.
[3] G. Paramasivam, N. Kayambu, A.M. Rabel, A.K. Sundramoorthy, A. Sundaramurthy, Anisotropic noble metal nanoparticles: synthesis, surface functionalization and applications in biosensing, bioimaging, drug delivery and theranostics, Acta Biomater. 49 (2017) 45–65.
[4] J. Boken, P. Khurana, S. Thatai, D. Kumar, S. Prasad, Plasmonic nanoparticles and their analytical applications: a review, Appl. Spectrosc. Rev. 52 (2017) 774–820.
[5] S. Sasidharan, D. Bahadur, R. Srivastava, Protein-poly(amino acid) nanocore-shell mediated synthesis of branched gold nanostructures for computed tomographic imaging and photothermal therapy of Cancer, ACS Appl. Mater. Interf. 8 (2016) 15889–15903.
[6] A.J. Blanch, M. Döblinger, J. Rodríguez-Fernández, Simple and rapid high-yield synthesis and size sorting of multibranched hollow gold nanoparticles with highly tunable NIR plasmon resonances, Small 11 (2015) 4550–4559.
[7] Z. Liu, Z. Yang, B. Peng, C. Cao, C. Zhang, H. You, Q. Xiong, Z. Li, J. Fang, Highly sensitive, uniform, and reproducible surface-enhanced raman spectroscopy from hollow Au-Ag alloy nanourchins, Adv. Mater. 26 (2014) 2431–2439.
[8] A. Guerrero-Martínez, S. Barbosa, I. Pastoriza-Santos, L.M. Liz-Marzán, Nanostars shine bright for you: colloidal synthesis, properties and applications of branched metallic nanoparticles, Curr. Opin. Colloid Interface Sci. 16 (2011) 118–127.
[9] J. Xie, Q. Zhang, J.Y. Lee, D.I.C. Wang, The synthesis of SERS-active gold nanoflower tags for in vivo applications, ACS Nano 2 (2008) 2473–2480.
[10] Y. Hsiangkuo, G.K. Christopher, H. Hanjun, M.W. Christy, A.G. Gerald, V.-D. Tuan, Gold nanostars: surfactant-free synthesis, 3D modelling, and two-photon photoluminescence imaging, Nanotechnology 23 (2012) 075102.
[11] A. Zaleska-Medynska, M. Marchelek, M. Diak, E. Grabowska, Noble metal-based bimetallic nanoparticles: the effect of the structure on the optical,

catalytic and photocatalytic properties, Adv. Colloid Interf. Sci. 229 (2016) 80–107.
[12] J. Prakash, R.A. Harris, H.C. Swart, Embedded plasmonic nanostructures: synthesis, fundamental aspects and their surface enhanced Raman scattering applications, Int. Rev. Phys. Chem. 35 (2016) 353–398.
[13] D. Jimenez de Aberasturi, A.B. Serrano-Montes, J. Langer, M. Henriksen-Lacey, W.J. Parak, L.M. Liz-Marzán, Surface enhanced raman scattering encoded gold nanostars for multiplexed cell discrimination, Chem. Mater. 28 (2016) 6779–6790.
[14] M. König, A. Radojcic, S. Schlücker, W. Xie, Label-free SERS monitoring of hydride reduction catalyzed by Au nanostars, J. Raman Spectrosc. 47 (2016) 1024–1028.
[15] P. Priecel, H. Adekunle Salami, R.H. Padilla, Z. Zhong, J.A. Lopez-Sanchez, Anisotropic gold nanoparticles: preparation and applications in catalysis, Chin. J. Catal. 37 (2016) 1619–1650.
[16] F. Hao, C.L. Nehl, J.H. Hafner, P. Nordlander, Plasmon resonances of a gold nanostar, Nano Lett. 7 (2007) 729–732.
[17] K.M. Mayer, J.H. Hafner, Localized surface plasmon resonance sensors, Chem. Rev. 111 (2011) 3828–3857.
[18] M.J. Walsh, S.J. Barrow, W. Tong, A.M. Funston, J. Etheridge, Symmetry breaking and silver in gold nanorod growth, ACS Nano 9 (2015) 715–724.
[19] Gold Nanomaterials at Work in Biomedicine, Chem. Rev. 115 (2015) 10410.
[20] L. Ma, Y. Huang, M. Hou, Z. Xie, Z. Zhang, Silver nanorods wrapped with ultrathin Al_2O_3 layers exhibiting excellent SERS sensitivity and outstanding SERS stability, Sci. Rep. 5 (2015) 12890.
[21] S. Schlücker, Surface-enhanced raman spectroscopy: concepts and chemical applications, Angew. Chem. 53 (2014) 4756–4795.
[22] J.-F. Li, Y.-J. Zhang, S.-Y. Ding, R. Panneerselvam, Z.-Q. Tian, Core-Shell nanoparticle-enhanced raman spectroscopy, Chem. Rev. 117 (2017) 5002–5069.
[23] K.D. Gilroy, A. Ruditskiy, H.-C. Peng, D. Qin, Y. Xia, Bimetallic nanocrystals: syntheses, properties, and applications, Chem. Rev. 116 (2016) 10414–10472.
[24] J.-J. Feng, L. Liu, H. Huang, A.-J. Wang, Poly(ionic liquid)-assisted one-pot synthesis of Au hyperbranched architectures for enhanced SERS performances, Sens. Actuat. B 238 (2017) 91–97.
[25] S. Sasidharan, D. Bahadur, R. Srivastava, Rapid one-pot, protein-mediated green synthesis of gold nanostars for computed tomographic imaging and photothermal therapy of cancer, ACS Sustain. Chem. Eng. 5 (2017) 10163–10175.
[26] Z. Cao, Q. Chen, J. Zhang, H. Li, Y. Jiang, S. Shen, G. Fu, B.-A. Lu, Z. Xie, L. Zheng, Platinum-nickel alloy excavated nano-multipods with hexagonal close-packed structure and superior activity towards hydrogen evolution reaction, Nat. Commun. 8 (2017) 15131.
[27] J.G. Weers, J.F. Rathman, F.U. Axe, C.A. Crichlow, L.D. Foland, D.R. Scheuing, R.J. Wiersema, A.G. Zielske, Effect of the intramolecular charge separation distance on the solution properties of betaines and sulfobetaines, Langmuir 7 (1991) 854–867.
[28] P. Pallavicini, G. Chirico, M. Collini, G. Dacarro, A. Donà, L. D'Alfonso, A. Falqui, Y. Diaz-Fernandez, S. Freddi, B. Garofalo, A. Genovese, L. Sironi, A. Taglietti, Synthesis of branched Au nanoparticles with tunable near-infrared LSPR using a zwitterionic surfactant, ChemComm. 47 (2011) 1315–1317.
[29] A.P. Gerola, P.F.A. Costa, F.H. Quina, H.D. Fiedler, F. Nome, Zwitterionic surfactants in ion binding and catalysis, Curr. Opin. Coll. Interf. Sci. 32 (2017) 39–47.
[30] A. Casu, E. Cabrini, A. Donà, A. Falqui, Y. Diaz-Fernandez, C. Milanese, A. Taglietti, P. Pallavicini, Controlled synthesis of gold nanostars by using a zwitterionic surfactant, Chem. Eur. J. 18 (2012) 9381–9390.
[31] X. Huang, M.A. El-Sayed, Plasmonic photo-thermal therapy (PPTT), Alexandria J. Med. 47 (2011) 1–9.
[32] L.C. Kennedy, L.R. Bickford, N.A. Lewinski, A.J. Coughlin, Y. Hu, E.S. Day, J.L. West, R.A. Drezek, A new era for cancer treatment: gold-nanoparticle-mediated thermal therapies, Small 7 (2011) 169–183.
[33] L. Cheng, C. Wang, L. Feng, K. Yang, Z. Liu, Functional nanomaterials for phototherapies of cancer, Chem. Rev. 114 (2014) 10869–10939.
[34] L.V. Nair, Y. Nagaoka, T. Maekawa, D. Sakthikumar, R.S. Jayasree, Quantum dot tailored to single wall carbon nanotubes: a multifunctional hybrid nanoconstruct for cellular imaging and targeted photothermal therapy, Small 10 (2014) 2771–2775.
[35] J. Ren, S. Shen, D. Wang, Z. Xi, L. Guo, Z. Pang, Y. Qian, X. Sun, X. Jiang, The targeted delivery of anticancer drugs to brain glioma by PEGylated oxidized multi-walled carbon nanotubes modified with angiopep-2, Biomaterials 33 (2012) 3324–3333.
[36] S. Su, J. Wang, J. Wei, R. Martínez-Zaguilán, J. Qiu, S. Wang, Efficient photothermal therapy of brain cancer through porphyrin functionalized graphene oxide, New J. Chem. 39 (2015) 5743–5749.
[37] Y. Jin, Engineering plasmonic gold nanostructures and metamaterials for biosensing and nanomedicine, Adv. Mater. 24 (2012) 5153–5165.
[38] J. Wang, Z. Zhou, F. Zhang, H. Xu, W. Chen, T. Jiang, A novel nanocomposite based on fluorescent turn-on gold nanostars for near-infrared photothermal therapy and self-theranostic caspase-3 imaging of glioblastoma tumor cell, Coll. Surf. B 170 (2018) 303–311.
[39] H. Chatterjee, D.S. Rahman, M. Sengupta, S.K. Ghosh, Gold Nanostars in plasmonic photothermal therapy: the role of tip heads in the thermoplasmonic landscape, The J. Phys. Chem. C 122 (2018) 13082–13094.
[40] Y. Tian, Y. Zhang, Z. Teng, W. Tian, S. Luo, X. Kong, X. Su, Y. Tang, S. Wang, G. Lu, pH-dependent transmembrane activity of peptide-functionalized gold nanostars for computed tomography/photoacoustic imaging and photothermal therapy, ACS Appl. Mater. Interf. 9 (2017) 2114–2122.
[41] A.G.M. da Silva, T.S. Rodrigues, S.J. Haigh, P.H.C. Camargo, Galvanic replacement reaction: recent developments for engineering metal nanostructures towards catalytic applications, ChemComm 53 (2017) 7135–7148.
[42] D. Joseph, H. Lee, Y.S. Huh, Y.-K. Han, Cylindrical core-shell tween 80 micelle templated green synthesis of gold-silver hollow cubic nanostructures as efficient nanocatalysts, Mater. Des. (2018).
[43] C.C. Huang, Z. Yang, H.-T. Chang, Synthesis of dumbbell-shaped Au−Ag core−shell nanorods by seed-mediated growth under alkaline conditions, Langmuir 20 (2004) 6089–6092.
[44] M.S. Bakshi, How surfactants control crystal growth of nanomaterials, Cryst. Growth Des. 16 (2016) 1104–1133.
[45] N. Pradhan, A. Pal, T. Pal, Silver nanoparticle catalyzed reduction of aromatic nitro compounds, Colloids Surf. A 196 (2002) 247–257.
[46] M. Guo, J. He, Y. Li, S. Ma, X. Sun, One-step synthesis of hollow porous gold nanoparticles with tunable particle size for the reduction of 4-nitrophenol, J. Hazard. Mater. 310 (2016) 89–97.
[47] M.A. Mahmoud, B. Garlyyev, M.A. El-Sayed, Determining the mechanism of solution metallic nanocatalysis with solid and hollow nanoparticles: homogeneous or heterogeneous, J. Phys. Chem. C 117 (2013) 21886–21893.
[48] D. Joseph, K.E. Geckeler, Surfactant-directed multiple anisotropic gold nanostructures: synthesis and surface-enhanced Raman scattering, Langmuir 25 (2009) 13224–13231.